Optics and Lasers in Engineering 161 (2023) 107336

Contents lists available at ScienceDirect

Optics and Lasers in Engineering

journal homepage: www.elsevier.com/locate/optlaseng

Fast and robust wave optics-based reconstruction protocol for Fourier lightfield microscopy

Nicolo Incardona [a,*], Angel Tolosa [a], Genaro Saavedra [a], Manuel Martinez-Corral [a], Emilio Sanchez-Ortiga [a,b]

[a] 3D Imaging and Display Laboratory, Department of Optics, Universitat de València, Burjassot, 46100, Spain
[b] School of Science, Universidad Europea de Valencia, Valencia, 46010, Spain

ARTICLE INFO

Keywords:
Fourier lightfield microscopy
FLMic
3D microscopy
3D Deconvolution
GPU

ABSTRACT

Fourier lightfield microscopy (FLMic) is a powerful technique to record 3D images of thick dynamic samples. Belonging FLMic to the general class of computational imaging techniques, its efficiency is determined by several factors, like the optical system, the calibration process, the reconstruction algorithm, or the computation architecture. In the case of FLMic the calibration and the reconstruction algorithm should be fully adapted to the singular features of the technique. To this end, and concerning the reconstruction, we discard the use of experimental PSFs, and propose the use of a synthetic one, which is calculated on the basis of paraxial optics and taking into account the equal influence of diffraction and pixelation. Using this quite simple PSF, performing the adequate calibration and finally implementing the algorithm in GPU, we demonstrate here the possibility of obtaining 3D images with good results in terms of resolution and strong improvement in terms of computation time. In summary, and aiming to accelerate the widespread of FLMic among microscopy users and researchers, we are proposing a fast protocol fully adapted to FLMic and that is very flexible and robust against any slight misalignment or against the change of any optical element.

1. Introduction

Lightfield microscopy (LMic) [1–4] is an emerging microscopy technique that is particularly suited to the acquisition of 3D images of thick dynamic samples. Its strength comes from its ability to capture a radiance map in only one shot. This ability has promoted the use of LMic in diverse applications [5–7]. However, its broad application to 3D imaging of dynamic specimens has slowed down due to some drawbacks that are inherent to LMic. We refer to the low resolution of captured images, the inhomogeneous resolution of reconstructed depth images, and the lack of lateral shift invariance, which greatly hinders the efficient application of deconvolution tools [8].

To overcome these problems, Fourier lightfield microscopy (FLMic) [9–11] was proposed. FLMic results from a change of paradigm, since the radiance map is sampled, not at the image plane, but at the Fourier plane. This is done by sub-sampling the aperture stop of a telecentric microscope objective, with the insertion of a microlens array (MLA). The resulting image consists of a set of orthographic views of the sample, each captured from a different viewing angle. Along the recent years, FLMic has been used for diverse applications in which both 3D information and time resolution are fundamental. This is the case of neural activity [12,13], single molecule localization [14], or particle imaging velocimetry [15], just to mention a few.

Lightfield imaging, and therefore FLMic, belongs to the family of computational-imaging techniques [16,17]. In fact, the 3D information of the sample is not registered directly (like in confocal microscopy or single plane illumination microscopy [18–20]), but it is extracted from the captured spatio-angular map. For this reason, lightfield microscopy has aroused interest in both optics and computer science research communities.

As for the reconstruction process, the first algorithms in FLMic were based on ray optics. For example, in [10], a classic back-propagation algorithm is used. Going one step further, in [21], a two-stage 3D reconstruction algorithm is reported, in which, first, a focal stack is computed with a classic back-propagation algorithm. Later, the focal stack, which conforms a 3D image, is deconvolved with a purely-geometric 3D reconstruction PSF using a Wiener-like filter. This method shows better results, providing optical sectioning for fluorescence samples. In [22],

* Corresponding author.
E-mail addresses: nicolo.incardona@uv.es (N. Incardona), angel.tolosa@uv.es (A. Tolosa), genaro.saavedra@uv.es (G. Saavedra), manuel.martinez@uv.es (M. Martinez-Corral), emilio.sanchez@uv.es (E. Sanchez-Ortiga).

https://doi.org/10.1016/j.optlaseng.2022.107336
Received 29 July 2022; Received in revised form 29 September 2022; Accepted 17 October 2022

the authors propose a geometrical reconstruction method that provides optical sectioning in real-time.

Ray optics techniques have demonstrated, then, to be able to reconstruct the 3D sample in a simple and fast way. We cannot ignore, however, that they omit the wave optics effects, which in microscopy are usually important. Then, wave optics-based methods are establishing themselves as the standard reconstruction methods, because they provide better lateral and axial resolution. One of the reasons is that, although FLMic has much larger depth of field (DOF) as compared to a conventional widefield microscope, usually the thickness of the sample observed is greater than the DOF of the system.

Wave optics-based methods usually rely on Richardson-Lucy deconvolution procedure. In the case of lightfield imaging, the 2D image captured by the sensor (that is, the collection of orthographic views) is iteratively deconvolved with the transverse sections of the 3D PSF of the optical system, to get an estimation of the 3D volume of the sample. This simple way of proceeding is very challenging in conventional LMic due to the lack of lateral shift invariance [8]. However, it is immediate in the case of FLMic due to his innate feature of lateral shift invariance. In some works that make use of an FLMic scheme [23,24], the 3D PSF is captured experimentally. In that case, and thanks to the lateral shift invariance, obtaining the 3D PSF of the system is easy, since one simply needs to capture a stack of images of a point object that is scanned only along the axial direction. Obviously, the experimental 3D PSF provides an accurate result, as the real features of the optical and the electronical components are taken into account.

The main drawback of using the experimental PSF is the lack of flexibility. Take into account that, in realistic experiments, it may be necessary to change some of the system components (e.g. the objective, or the filter cube) depending on the kind of sample. Or it may even happen that some component is mechanically misaligned due to use. In such cases, the 3D PSF capture should be repeated. Then, it makes sense, as suggested in [25], to compute a synthetic 3D PSF on the basis of a wave optics propagation model. Obviously, the synthetic 3D PSF is not as accurate as the experimentally captured one. In fact, it does not take into account the tolerance of the optical components and the possible mechanical misalignments of the set-up. However, as we will explain in Section 2, the particularities of the FLMic systems make small inaccuracies tolerable.

Even though opting for a synthetic 3D PSF represents a simplification of the real case, the process has remained still challenging. This is the case of Refs. [23,25], where the 3D PSF is calculated starting from the Debye model for a high numerical aperture (NA) objective and ignores the pixelation influence. This way of calculating the synthetic PSF is accurate in conventional microscopy, but does not take into account the particularities of FLMic. Specifically, the high NA assumption does not hold for FLMic, where the effective NA is only a fraction of the nominal one. Thus, that model brings unnecessary computational complexity, that slows down the PSF calculation. Also, such calculated PSF does not take into account the geometric PSF associated to the pixels size and shape. In addition, in [25], the calibration process relies on the capture of a plane sample placed exactly at the object plane of the microscope objective. However, placing the sample at the object plane of an FLMic is very difficult, due to its extended DOF.

The aim of this paper is to demonstrate that, in case of FLMic, the reconstruction protocol can be simplified, providing faster computations and higher efficiency. Due to its subsampling and shift-invariant feature, in FLMic the PSF is well defined and has a paraxial nature. Besides, since the size of the diffractive PSF is comparable with the sensor pixel size, any (x, y) section of the synthetic 3D PSF is actually composed by only a few pixels. In addition, the proposed calibration method is based on the capture of a blank image, which makes it much more robust. Finally, the algorithm is implemented in GPU, to allow the use of FLMic in dynamic processes. All these features provide the proposed FLMic protocol with improved flexibility, robustness and computation speed.

2. Materials and methods

2.1. Image formation model

The optical set-up of an FLMic is shown in Fig. 1. A $4f$ relay system is used to conjugate the aperture stop with the MLA. The functioning of FLMic has been largely discussed and the image formation has been analyzed from both ray optics and wave optics points of view. In [23], the wavefront is computed at the intermediate image plane, using the Debye model for high NA objective [26]. In [25], the same model is also used, this time to compute the wavefront at the aperture stop. In both image formation models, the wavefront is then propagated to the sensor plane, through the different optical components. Both models provide a very accurate estimation of the diffractive 3D PSF of the system. However, we demonstrate here that these models are exceedingly sophisticated, since they add unnecessary complexity load, slowing down the computation of the PSF.

Based on the optical nature of FLMic, we make some considerations to simplify the image formation model. The first is that the effective NA of the objective is reduced, as the aperture stop is sub-sampled by the MLA. The effective NA can be expressed as:

$$NA_{eff} = \frac{NA_{Ob}}{N}, \tag{1}$$

with

$$N = \frac{f_2\,\Phi_{AS}}{f_1\,p}, \tag{2}$$

where NA_{Ob} is the NA of the microscope objective, N is the number of microlenses that fit into the diameter, Φ_{AS}, of the objective aperture stop, and p is the pitch of the MLA.

The second consideration is that, in fact, an FLMic is an optical microscope that works with very low magnification. Specifically, the total lateral magnification between the object plane and the sensor plane is

$$M_{Tot} = \frac{f_{MLA} f_1}{f_{Ob} f_2}. \tag{3}$$

Taking into account that, for a correct functioning of an FLMic, a minimum value of $N = 3$ is required, in most realistic geometries, M_{Tot} is confined to values smaller than 3.0 [27]. As a consequence, the Airy disk, whose radius at the image plane is

$$r'_{Airy} = 0.61\frac{\lambda}{NA_{eff}} M_{Tot}, \tag{4}$$

is clearly undersampled. As an example, consider the case of an FLMic consisting of a 40×, $NA = 0.4$ objective, and MLA with $f_{MLA} = 6.4\ mm$ and $p = 1.0\ mm$. In this case the required value of $N = 3.0$ is obtained for $M_{Tot} = 1.72$. Then, we obtain $r'_{Airy} = 4.7$ µm, which is totally comparable to a normal pixel size. As a consequence, the sampled 3D PSF is composed, laterally, by only a few pixels.

Let us open a bracket here to state that one should not worry about the low magnification values, since the key feature of microscopes is not magnification, but spatial resolution.

For the exposed reasons, it is apparent that using the Debye model for high NA objectives adds exceeding computational cost to the 3D PSF calculation and provides no benefit in terms of spatial resolution.

Let us consider the simplified model of FLMic shown in Fig. 2. The effect of diffraction is the same for all the microlenses of the MLA. Regarding the geometric effect, as is well known from past works about FLMic [10,23,25], in the lateral microlenses the image of a point source located on the optical axis is formed at a distance from the central pixel (of the corresponding elemental image) that depends on the point axial depth, as measured from the object plane. Consequently, and due to the lateral shift-invariant feature, the PSF of a lateral microlens is the same as that of the central microlens, but with a lateral displacement (or disparity) that depends on the point axial depth. Therefore, modelling the light propagation through all the optical components also adds redundant complexity. To compute the 3D PSF of the FLMic, one only needs

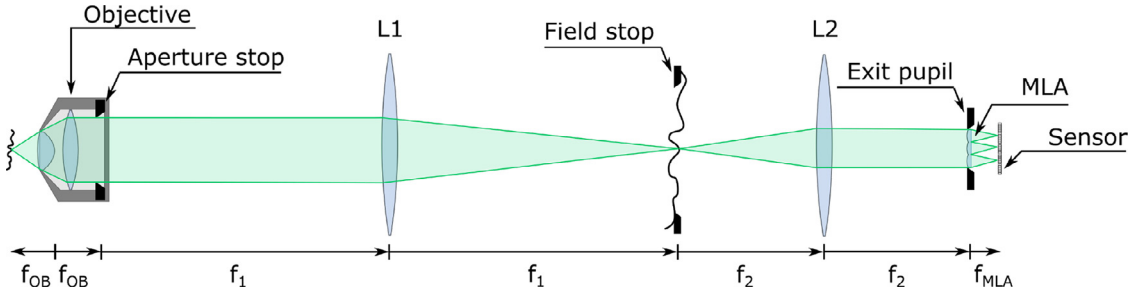

Fig. 1. Fourier lightfield microscope optical set-up. The lenses L1-L2 form a telecentric relay that conjugates the microlens array (MLA) with the aperture stop. The exit pupil is the image of the aperture stop. The field stop is placed at the plane of the intermediate image, in order to avoid the overlapping between the elemental images (EIs) formed by the microlenses.

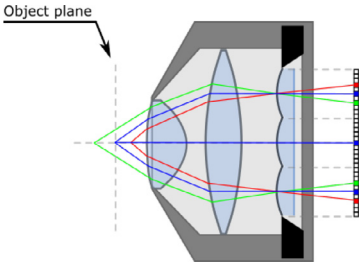

Fig. 2. In the lateral microlenses of an FLMic, the image of an axial point source is displaced from the center of the elemental image. The shift depends on the depth of the point source.

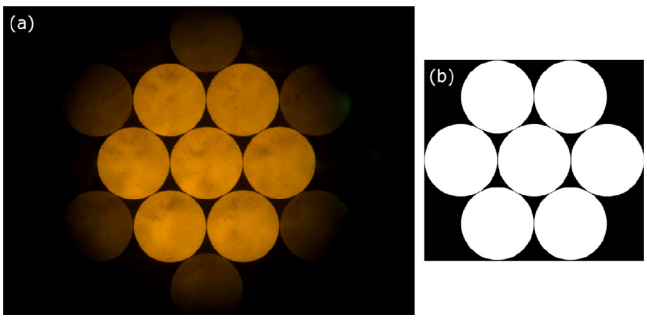

Fig. 3. The images used to calibrate the FLMic. (a) The blank image captured with the real system. (b) The binary image created to find the translation and rotation of the MLA.

to compute the 3D PSF of the central microlens and to know the exact positions of the lateral microlenses.

2.2. Calibration

To build the 3D PSF of the FLMic, it is necessary to know exactly the position of the EIs, that is, the location of the central pixel behind each microlens. In fact, an inaccurate calibration can lead to reconstruction errors that can range from object translation and small artefacts (for small inaccuracies in the calibration of one or two microlenses), to the failure to reconstruct the sample (in case of bigger errors in the calibration). It is difficult to correlate the reconstruction errors with the accuracy of the calibration, but we can assume that an error of maximum 1 pixel in the horizontal and vertical direction, in maximum two microlenses out of seven, can be tolerated, because it leads to negligible reconstruction artefacts.

To know the position of the EIs with the maximum accuracy, we designed an easy and robust calibration method. This method is based on the capture of a so-called blank image; that is, an image obtained illuminating directly the objective without inserting any sample. The image obtained is an array of circles, whose centers correspond to the central pixel of each EI. In Fig. 3(a), an example of blank image is shown.

Knowing the optical set-up parameters (pitch of the MLA, pixel size, etc.) and the geometry of the MLA (orthogonal or hexagonal arrangement), a binary image is created, with the same characteristics of the real blank image captured with the system. In the binary image, the central circle is placed exactly at the center of the image and the lateral EIs' centers are located on a perfectly horizontal line. In Fig. 3(b), the binary image created to calibrate the system of Fig. 3(a) is shown.

Both images are used to extract the translation and rotation of the MLA with respect to the sensor. First, a correlation matrix of both is calculated, and the location of the maximum is found. This location corresponds to the (x, y) translation of the MLA with respect to the center of the sensor. Then, the binary image is rotated by a constant angle, in a certain range of angles. A correlation matrix between the blank image and every rotated binary image is calculated: the correlation matrix having the highest maximum value corresponds to the rotation angle of the MLA. Once the translation and rotation of the MLA are found, it is possible to calculate the coordinates of the centers of the EIs.

As the centers of the microlenses with respect to the sensor only vary if the MLA or the sensor are changed (or moved), the calibration process only needs to be repeated in these cases. In the case that the microscope objective or the relay lenses were changed and the number of elemental images N changes, it would be still possible to calculate the coordinates without repeating the calibration, as the translation and the rotation would remain the same. In fact, to avoid the calculation of the coordinates at every execution, we save one file containing the coordinates of the centers for every possible value of N. Hence, at every execution of the reconstruction algorithm, it is sufficient to read the coordinates from this file.

2.3. The computation of the 3D PSF

As mentioned in Section 2.1, the first step is to generate the 3D PSF of the central microlens. With all the parameters of the optical system, and choosing the axial step (i.e., the axial distance between the slices of the 3D PSF), the 3D PSF of the central microlens is generated, based on Fraunhofer diffraction [26] and taking into account the pixel shape and size. It consists of an array of 2D images, each one containing the impulse response to a point source axially displaced by a constant distance (that we call axial step).

Once we have the 3D PSF of the central microlens, we can build the entire FLMic 3D PSF. To do so, for every microlens we need to calculate the shift of the Airy disk at every PSF slice. This shift can be expressed as

$$\mathbf{s} = \frac{z}{\Delta_z}\mathbf{d}, \tag{5}$$

where **s** is the (x, y) vector of the pixel shift, z is the distance of the PSF slice from the reference object plane, Δ_z is the axial distance related to a 1-pixel shift, and **d** is the vector containing the normalized distance (in pixels) of that given microlens to the central one. As demonstrated in [10], Δ_z is

$$\Delta_z = \frac{f_{MLA}}{p} \frac{\delta_{px}}{M_{Tot}^2}, \tag{6}$$

where δ_{px} is the pixel size.

As an example, we want to generate the 3D PSF of the FLMic used in Fig. 3. Let us suppose that for this FLMic, we have $\Delta_z = 5$ µm and that we generated the 3D PSF of the central microlens, choosing an axial step equal to Δ_z. Let us consider the rightmost microlens. Supposing that this microlens has its center at the same y coordinate as the central microlens, we have $\mathbf{d} = (1, 0)$. For the slice at $z = 0$ µm (the reference object plane), we have $\mathbf{s} = (0, 0)$, so the PSF of the rightmost microlens at this plane is identical to that of the central microlens. For the slice at $z = +5$ µm (5 µm closer to the objective lens), we have $\mathbf{s} = (1, 0)$. So, we take the corresponding PSF slice of the central microlens and we copy it into the rightmost EI, displacing it 1 pixel to the right. For the slice at $z = +10$ µm, we take the corresponding PSF slice of the central microlens and we copy it into the rightmost EI, displacing it 2 pixels to the right. For the PSF slices having negative depth (further from the objective lens than the reference object plane), the shift of the PSF in the rightmost microlens, with respect to the central pixel of the corresponding EI, would be to the left.

Applying Eq. (5) to every microlens, at all the 3D PSF slices, the 3D PSF of the FLMic is generated. The result is similar to that of Fig. 5(c), where we show the maximum intensity projection of the stack containing the 3D PSF of the FLMic used for capturing the sample of Fig. 5.

Given the image captured and the 3D PSF of the FLMic, the iterative Richardson-Lucy deconvolution algorithm is applied, to estimate the volume of the sample. The resulting estimation is a 3D discrete volume, in which the (x, y) spacing between the voxels is equal to the pixel size in the object space $\left(\frac{\delta_{px}}{M_{Tot}}\right)$ and the z spacing is equal to the axial step chosen.

The whole algorithm, including the calibration, the 3D PSF generation and the 3D reconstruction, is implemented in C++.

3. Results and discussion

3.1. Spatial resolution

To demonstrate the correct functioning of our method, we imaged a USAF 1951 resolution target. The target was placed at the object plane and at -50 µm from the object plane, to test the performances of the reconstruction method at different depths. The object was illuminated with brightfield illumination. The parameters of the FLMic used for capturing all the samples shown in the paper are given in Table 1. Take into account that the total DOF of the FLMic used to image the USAF target is about 72 µm. Thus, the plane at -50 µm from the object plane is out of the DOF of the FLMic.

We used our algorithm to reconstruct the sample and we compared the results with those obtained with the algorithm of [25] (without super-resolution). The parameters of the reconstruction are also given in Table 1. All the reconstructions, for all the samples, were performed on a Notebook MSI GL 63 8RC, equipped with 8th Gen. Intel® Core™ i7 processor, 16 GB RAM and NVIDIA GeForce® GTX 1050 with 4 GB DDR5 GPU and were made with 10 iterations of the Richardson-Lucy algorithm. The results of both algorithms are shown in Fig. 4. Fig. 4(a) shows the results for the target placed at the object plane, while (b) shows the results for the target placed at -50 µm. As expected, the resolution for the reconstruction of Fig. 4(b) is worse than that of (a). This is because, in the case of (b), the object was out of the DOF of the FLMic, as mentioned before. If we compare the results of both algorithms, at both depths, we note that the intensity profiles of all the elements are almost identical. This means that the performances of our method equalize those of [25], in terms of lateral resolution. Therefore, we can conclude that the assumptions made in Section 2 are appropiate and that the simplified image formation model proposed does not lead to a worsening in the quality of reconstruction. If we focus our attention on the image of the resolution target reconstructed with the algorithm of [25], inside the white square at the top of the image and inside the lines of the low resolution elements, some reconstruction artefacts can be noted. The same does not occur in the image of the resolution target reconstructed with our algorithm. These artefacts might be due to a slight error in the calibration.

Table 1
The table contains the data of the FLMic used for imaging each sample and the parameters used for the reconstruction. λ_{BF} is the wavelength of the barrier filter used. For the USAF target, this data is not included, as it was imaged with brightfield illumination. *z-step* is the axial step, that is the distance between the slices of the 3D PSF (and, consequently, the reconstructed volume). *z range* is the total volume of reconstruction.

Sample	USAF	Sphere	Hydrogel
f_{Ob}	10.0 mm	4.5 mm	9.0 mm
Φ_{AS}	10.0 mm	5.4 mm	7.2 mm
$\frac{f_2}{f_1}$	0.50	0.55	0.55
p	1.00 mm	1.00 mm	1.00 mm
f_{MLA}	6.4 mm	6.4 mm	7.9 mm
δ_{px}	2.2 µm	2.2 µm	2.2 µm
λ_{BF}	Brightfield	455 nm	420 nm
z-step	8.54 µm	2.13 µm	6.94 µm
z range [µm]	[-50.0, 0]	[-21.3, 34.1]	[-138.8, 138.8]

3.2. 3D sample reconstruction

Also, we tested the algorithm reconstructing the volume of two different 3D samples, observed with different FLMic configurations.

The first sample is the "Sphere" pattern of the Argo-HM test from Argolight. The pattern consists of three circles of 50 µm diameter. The circles are placed on three orthogonal planes, representing the equator and two meridians of a sphere. In Fig. 5(a), the image captured with the FLMic is shown, which consists of 7 elemental images in 2-3-2 configuration (two EIs in the top and the bottom line and three EIs in the central line). In Fig. 5(b), (c) and (d), we show some different image of the computed PSF. In Fig. 5(d), the 3D PSF of the FLMic is shown from a side view. In the top and bottom lines, two identical PSFs can be noted. Likewise, in the central line, three identical PSFs can be noted. This is because the MLA is rotated with respect to the sensor, so the center of each PSF has different y coordinates. For this reason, they can be all seen from a side view. Finally, in Fig. 5(e), the sample reconstruction at different depths is shown. We can see that the algorithm is capable of reconstructing the shape of the sphere, providing good optical sectioning. The distance between the first plane and the last plane in which non-zero signal of the sample is detected is about 51 µm, which is practically equal to the diameter of the sphere. In addition, the central meridian is exactly at half this distance, which confirms the precision of the volumetric estimation.

The second specimen is a sample of hydrogel with embedded fluorescent cells. The image captured is shown in Fig. 6(a). In this image, the effect of scattering is evident from the strong background. Yet, the algorithm is able to reconstruct the 3D sample. In fact, in FLMic, ballistic photons (the photons that travel on a straight line, passing through a scattering medium) are the only ones that follow the image formation model presented in Section 2.1. In Fig. 6(b), the sample reconstructed at different depths is shown. As mentioned before, the algorithm is capable of reconstructing the 3D volume despite the background. To further improve the quality of the 3D reconstruction, we applied the background

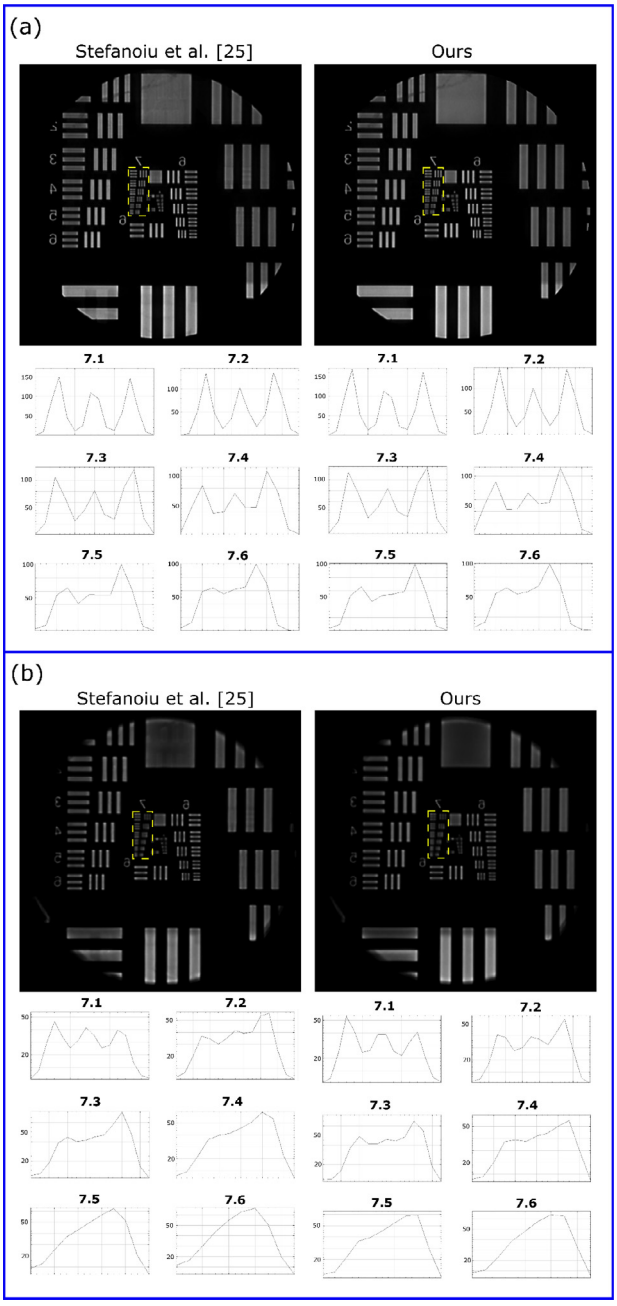

Fig. 4. (a) Reconstruction of the USAF 1951 resolution target placed at the object plane, with both the algorithm of [25] and ours. The intensity profiles of all the elements of group 7 are shown for both algorithms. (b) Reconstruction of the USAF target placed at -50 μm from the object plane, with both the algorithm of [25] and ours. The intensity profiles of all the elements of group 7 are shown below. Here, the resolution is worse than in (a), because the USAF was placed outside the DOF of the FLMic.

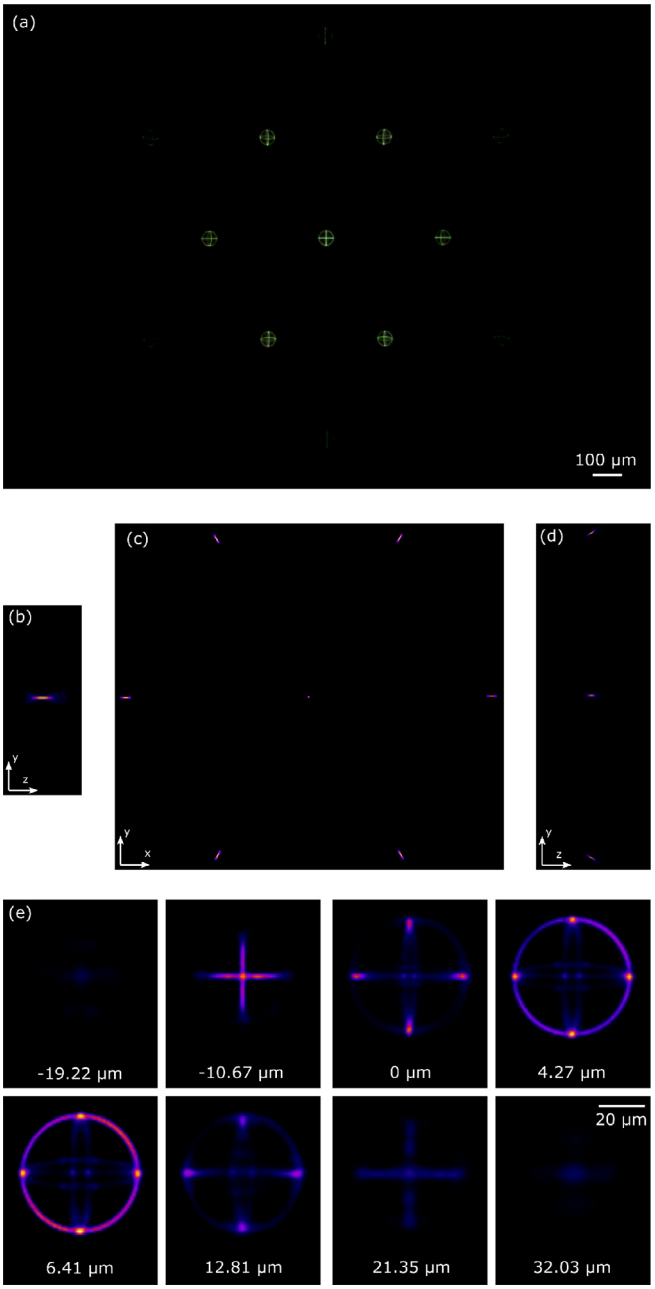

Fig. 5. (a) The image of the "Sphere" pattern of the Argo-HM test, captured with the FLMic, consisting of 7 total elemental images. (b) The 3D PSF of the central microlens from a side view. (c) The maximum intensity projection of the 3D PSF of the FLMic. (d) The 3D PSF of the FLMic from a side view. (e) The sample reconstructed at different depths. As can be seen from these images, the reconstruction method provides good optical sectioning.

subtraction method mentioned in [28]. We applied this method to the image of Fig. 6(a): the result is shown in Fig. 6(c). In Fig. 6(d), we show the comparison between the original central EI, and the central EI after applying the background subtraction. Finally, in Fig. 6(e) and (f), the volume reconstruction are shown for both the original and background-subtracted images, respectively. These volume visualizations were obtained with the "3D Project" function of ImageJ. A spacing of 5 pixels was applied between each reconstruction slice, to respect the ratio between the voxels' spacing in (x, y) and in z. Let us focus on the top views of both volume reconstructions. In the case of the original image reconstruction (Fig. 6(e)), a geometrical artefact can be noted around each reconstructed cell, with a hexagonal pattern similar to that of the MLA. In the case of the background-subtracted image reconstruction, this artefact is not present. On the other hand, the drawback of the background subtraction procedure is that it could remove the useful signal of the cells of deeper layers. This is because their images have lower contrast and bigger diameter respect to that of the cells of superficial layers, so they might be removed by the top-hat filtering. This effect can be noted comparing the side views of the volumes: in the side views of Fig. 6(f), some cells at the bottom of the volume are missing.

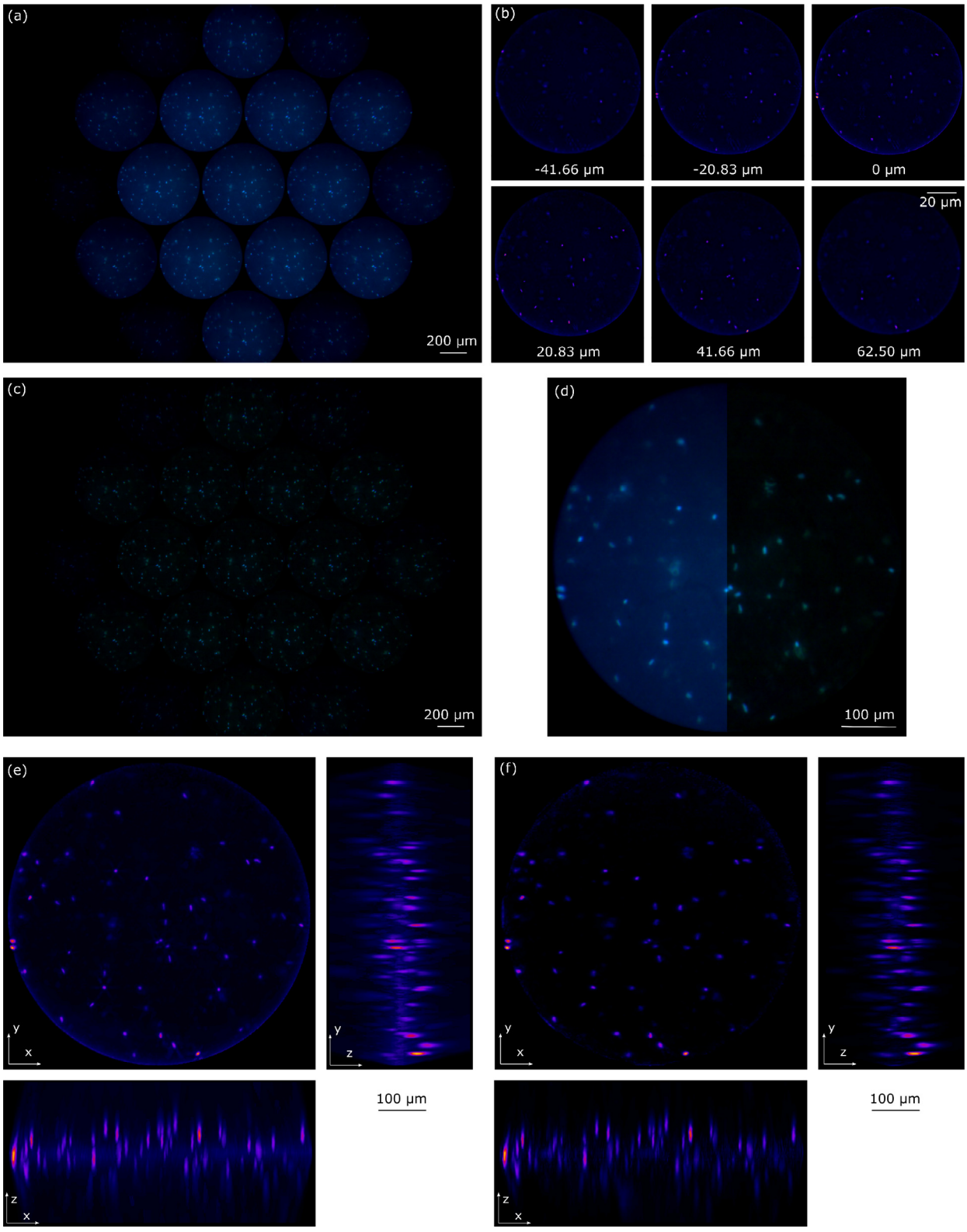

Fig. 6. (a) The image of a hydrogel sample with fluorescent cells, captured with the FLMic. The complete EIs are 7, while the other ones are only partially illuminated, as they do not fit into the exit pupil. (b) The sample reconstructed at different depths. (c) The image processed to subtract the background. (d) The difference between the central EI before (half left) and after (half right) the background subtraction. (e) The reconstructed volume from top view and two side views. To compute this volume, the deconvolution algorithm was applied to the original image (without subtracting the background). (f) The reconstructed volume from the top view and two side views, computed from the background-subtracted image.

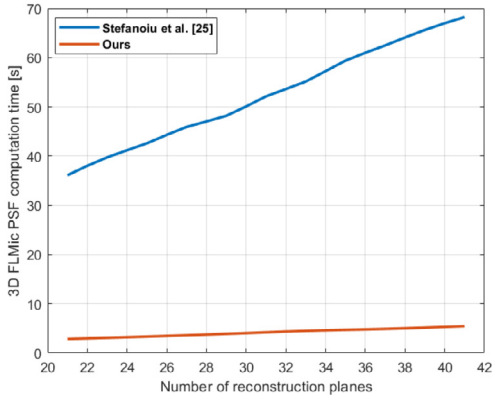

Fig. 7. The comparison between the time taken by our algorithm and that of [25] to compute the 3D PSF of an FLMic. The curves were generated measuring the time taken when the number of reconstruction slices varies from 21 to 41. Our algorithm is 12.5 times faster than that proposed in [25].

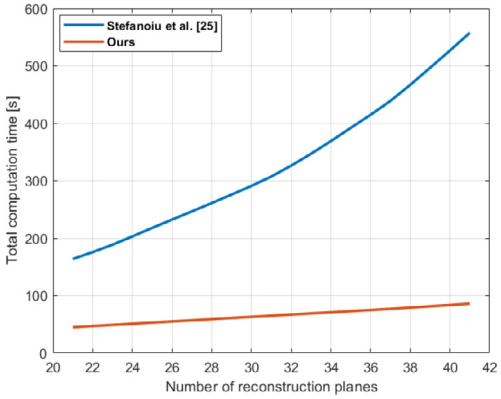

Fig. 8. The comparison between the total time taken by our algorithm and that of [25] to compute the 3D reconstruction of the sample. The curves were generated measuring the time taken when the number of reconstruction slices varies from 21 to 41. Our algorithm is minimum 3.6 times faster than [25] and the improvement increases for higher number of reconstruction slices.

3.3. Computation time

To demonstrate the improvement in the computation time given by the proposed method, we compared the computation times of [25] and those of our algorithm.

First, we measured the time needed by the different calibration methods. For the algorithm of [25], it was 145.9 seconds, while for our algorithm it was 3.8 seconds. Therefore, the implementation of our calibration method is much faster. In addition, it is much more robust. In fact, the calibration of [25] is based on the capture of a sample placed exactly on the object plane. As mentioned in Section 1, placing an object at the object plane is very difficult in FLMic, due to its large DOF.

Then, we measured the time taken by both algorithms to generate the 3D PSF of the FLMic. The 3D PSF computed for this test is that of the FLMic system used to image the hydrogel sample. The algorithm was tested varying the number of reconstruction slices by a constant step of 2, in a range from 21 to 41. In Fig. 7 we show the resulting curves for both algorithms. Both curves show a linear dependence on the number of reconstruction slices. The time taken from our algorithm goes from 2.853 seconds (for 21 slices) to 5.468 seconds (for 41 slices). The slope is approximately 0.13 seconds per reconstruction slice. The time taken from the algorithm of [25] goes from 36.115 seconds (for 21 slices) to 68.235 seconds (for 41 slices). The slope is 1.61 seconds per reconstruction slice, approximately. The improvement provided by our method is evident: our algorithm is 12.5 times faster generating the 3D PSF. This improvement is obviously due to the 3D PSF generation based on the simplified image formation model explained in Section 2.

The same experiment was repeated to extract the total computation time of both algorithms. This is the global execution time, including the 3D PSF generation, but excluding the calibration process. In fact, the calibration is only needed when the MLA or the sensor are changed or misaligned. So, we chose to exclude it from the total computation time, to make the comparison more fair. The result is shown in Fig. 8. Also in this case, the curve for our algorithm shows a linear dependence on the number of reconstruction slices. The total execution time goes from 45 seconds (for 21 slices) to 86 seconds (for 41 slices) with a slope of 2.05 seconds per slice. In contrast, the curve for the algorithm of [25] shows a quadratic dependence. The computation time measured goes from 163 seconds (for 21 slices) to 558 seconds (for 41 slices). Also in this case, the improvement given by our algorithm is clear. Specifically, in the range of reconstruction slices considered, our algorithm is 3.6 times faster in the case of 21 reconstruction slices and 6.5 times faster in the case of 41 reconstruction slices. While part of this improvement is due to the acceleration in the 3D PSF generation, the main contribution is given by the GPU implementation of the Richardson-Lucy deconvolution. Hence, the performances of the algorithm would be further improved if executed on a workstation with a better GPU.

4. Conclusions

In this paper we have presented a fast and robust 3D reconstruction protocol for Fourier lightfield microscopy. We have demonstrated that a synthetic PSF based on a simplified image formation model helps to speed up the 3D PSF generation. Other part of the protocol is the robust calibration procedure prior to the 3D PSF generation. Besides, we have demonstrated experimentally that the overall method provides a resolution similar to that obtained with a much more sophisticated algorithm and also that it is able to reconstruct 3D samples with high precision and optical sectioning. Finally, we showed that, implementing the algorithm in GPU, the computation time invested for the whole process (including the 3D PSF generation and the reconstruction algorithm execution), is much shorter than previous ones, while providing the same reconstruction quality. We believe that this accelerated processing speed, together with the single-shot nature of FLMic, can facilitate the widespread of FLMic among microscopy users and researchers.

Declaration of Competing Interest

The authors declare that they have no known competing financial interests or personal relationships that could have appeared to influence the work reported in this paper.

CRediT authorship contribution statement

Nicolo Incardona: Conceptualization, Data curation, Investigation, Methodology, Software, Validation, Visualization, Writing – original draft. **Angel Tolosa:** Funding acquisition, Investigation, Resources, Supervision. **Genaro Saavedra:** Formal analysis, Funding acquisition, Resources, Supervision. **Manuel Martinez-Corral:** Funding acquisition, Formal analysis, Methodology, Supervision, Writing – review & editing. **Emilio Sanchez-Ortiga:** Formal analysis, Methodology, Project administration, Supervision.

Acknowledgements

This research was funded by Grant RTI2018-099041-B-I00, which is co-founded by the Ministerio de Ciencia, Innovacion y Universidades (Spain), by the European Regional Development Fund, and by Generalitat Valenciana (Spain) under Grant PROMETEO/2019/048.

References

[1] Levoy M, Ng R, Adams A, Footer M, Horowitz M. Light field microscopy. In: ACM SIGGRAPH 2006 Papers; 2006. p. 924–34.
[2] Llavador A, Scrofani G, Saavedra G, Martinez-Corral M. Large depth-of-field integral microscopy by use of a liquid lens. Sensors 2018;18(10):3383.
[3] Skocek O, Nöbauer T, Weilguny L, Martínez Traub F, Xia CN, Molodtsov MI, Grama A, Yamagata M, Aharoni D, Cox DD, et al. High-speed volumetric imaging of neuronal activity in freely moving rodents. Nature Methods 2018;15(6):429–32.
[4] Li H, Guo C, Kim-Holzapfel D, Li W, Altshuller Y, Schroeder B, Liu W, Meng Y, French JB, Takamaru K-I, et al. Fast, volumetric live-cell imaging using high-resolution light-field microscopy. Biomed Opt Express 2019;10(1):29–49.
[5] Prevedel R, Yoon Y-G, Hoffmann M, Pak N, Wetzstein G, Kato S, Schrödel T, Raskar R, Zimmer M, Boyden ES, et al. Simultaneous whole-animal 3d imaging of neuronal activity using light-field microscopy. Nature Methods 2014;11(7):727–30.
[6] Wagner N, Norlin N, Gierten J, de Medeiros G, Balázs B, Wittbrodt J, Hufnagel L, Prevedel R. Instantaneous isotropic volumetric imaging of fast biological processes. Nature Methods 2019;16(6):497–500.
[7] Pégard NC, Liu H-Y, Antipa N, Gerlock M, Adesnik H, Waller L. Compressive light–field microscopy for 3d neural activity recording. Optica 2016;3(5):517–24.
[8] Zhang Y, Lu Z, Wu J, Lin X, Jiang D, Cai Y, Xie J, Wang Y, Zhu T, Ji X, et al. Computational optical sectioning with an incoherent multiscale scattering model for light-field microscopy. Nature Commun 2021;12(1):1–11.
[9] Llavador A, Sola-Pikabea J, Saavedra G, Javidi B, Martínez-Corral M. Resolution improvements in integral microscopy with fourier plane recording. Opt Express 2016;24(18):20792–8.
[10] Scrofani G, Sola-Pikabea J, Llavador A, Sanchez-Ortiga E, Barreiro J, Saavedra G, Garcia-Sucerquia J, Martínez-Corral M. Fimic: design for ultimate 3d-integral microscopy of in-vivo biological samples. Biomed Opt express 2018;9(1):335–46.
[11] Hua X, Liu W, Jia S. High-resolution fourier light-field microscopy for volumetric multi-color live-cell imaging. Optica 2021;8(5):614–20.
[12] Cong L, Wang Z, Chai Y, Hang W, Shang C, Yang W, Bai L, Du J, Wang K, Wen Q. Rapid whole brain imaging of neural activity in freely behaving larval zebrafish (danio rerio). Elife 2017;6.
[13] Yoon Y-G, Wang Z, Pak N, Park D, Dai P, Kang JS, Suk H-J, Symvoulidis P, Guner-Ataman B, Wang K, et al. Sparse decomposition light-field microscopy for high speed imaging of neuronal activity. Optica 2020;7(10):1457–68.
[14] Sims RR, Rehman SA, Lenz MO, Benaissa SI, Bruggeman E, Clark A, Sanders EW, Ponjavic A, Muresan L, Lee SF, et al. Single molecule light field microscopy. Optica 2020;7(9):1065–72.
[15] Huck P., Fort C., Bardet P.. Molecular tagging velocimetry techniques in wall-bounded turbulent flows.
[16] Martínez-Corral M, Javidi B. Fundamentals of 3d imaging and displays: a tutorial on integral imaging, light-field, and plenoptic systems. Adv Opt Photonic 2018;10(3):512–66.
[17] Javidi B, Carnicer A, Arai J, Fujii T, Hua H, Liao H, Martínez-Corral M, Pla F, Stern A, Waller L, et al. Roadmap on 3d integral imaging: sensing, processing, and display. Opt Express 2020;28(22):32266–93.
[18] Sheppard C, Cogswell C. Three-dimensional image formation in confocal microscopy. J Microsc 1990;159(2):179–94.
[19] Kino GS, Corle TR. Confocal scanning optical microscopy and related imaging systems. Academic Press; 1996.
[20] Huisken J, Swoger J, Del Bene F, Wittbrodt J, Stelzer EH. Optical sectioning deep inside live embryos by selective plane illumination microscopy. Science 2004;305(5686):1007–9.
[21] Sánchez-Ortiga E, Llavador A, Saavedra G, García-Sucerquia J, Martínez-Corral M. Optical sectioning with a wiener-like filter in fourier integral imaging microscopy. Appl Phys Lett 2018;113(21):214101.
[22] Sanchez-Ortiga E, Scrofani G, Saavedra G, Martínez-Corral M. Optical sectioning microscopy through single-shot lightfield protocol. IEEE Access 2020;8:14944–52.
[23] Guo C, Liu W, Hua X, Li H, Jia S. Fourier light-field microscopy. Opt Express 2019;27(18):25573–94.
[24] Liu FL, Kuo G, Antipa N, Yanny K, Waller L. Fourier diffuserscope: single-shot 3d fourier light field microscopy with a diffuser. Opt Express 2020;28(20):28969–86.
[25] Stefanoiu A, Scrofani G, Saavedra G, Martínez-Corral M, Lasser T. What about computational super-resolution in fluorescence fourier light field microscopy? Opt Express 2020;28(11):16554–68.
[26] Gu M. Advanced optical imaging theory, vol 75. Springer Science & Business Media; 2000.
[27] Galdón L, Saavedra G, Garcia-Sucerquia J, Martínez-Corral M, Sánchez-Ortiga E. Fourier lightfield microscopy: a practical design guide. Appl Opt 2022;61(10):2558–64.
[28] Xue Y, Davison IG, Boas DA, Tian L. Single-shot 3d wide-field fluorescence imaging with a computational miniature mesoscope. Sci Adv 2020;6(43):eabb7508.

Nicoló Incardona received his B.Eng. and M.Sc. degrees in Electronic Engineering from Polytechnic University of Milan in 2013 and 2016, respectively. He developed his master's thesis at Polytechnic University of Valencia. Since 2017 he has been working with the 3D Imaging and Display Laboratory of University of Valencia. Since 2018 he has been working in Digital Optical Imaging Technologies S.L., a spin-off company of the University of Valencia, developing the plenoptic eyepiece. His research interests are lightfield microscopy, image processing and 3D display.

Ángel Tolosa received the B. Sc and M. Sc in Physics from the University of Valencia in 2001 and 2009 respectively. From 2002 to 2015 he worked at the Technological Institute of Optics, Colour and Imaging in Valencia, Spain, first in fields as Metrology, Colour and Optical Properties of Materials, and later in Optical Design and 3D Imaging and Display. In 2016 he has been working on the design of a new scleral contact lens with the Group of Optics and Visual Perception, University of Alicante. Angel started to collaborate with the 3D Imaging and Display Laboratory in 2009 as external member. He received his PhD degree in 2022. He is a founding associate of Digital Optical Imaging Technologies, S.L., spin-off company of the University of Valencia, which commercializes the plenoptic eyepiece. His research interests include 3D display and visualization, 3D image capturing and optical design.

Genaro Saavedra received the BSc and PhD (cum laude) degrees in Physics from the University of Valencia, Spain, in 1990 and 1996, respectively. He is currently a Full Professor and, since 1999, he is the co-leader of the 3D Imaging and Display Laboratory at that University. His research interests are optical diffraction, plenoptic/integral imaging techniques, and 3D high-resolution optical microscopy. He has supervised on these topics 12 PhD theses (2 of them honored with the Best Thesis Award). He has published about 130 technical articles on these topics in major journals. He has contributed in more than 90 conference proceedings, including more than 50 invited/keynote presentations. He has filed 15 patents on 3D display and imaging techniques. He is a founding associate of the spin-off company Digital Optical Imaging Technologies, S.L.

Manuel Martnez-Corral received the Ph. D. degree in Physics (Best Thesis Award) from the University of Valencia in 1993. Currently Full Professor of Optics at the University of Valencia, he co-leads the "3D Imaging and Display Laboratory". He was elected Fellow of the SPIE and Fellow of the OSA in 2010 and 2017, respectively. His research interest includes resolution protocols in 3D scanning microscopy, and 3D imaging and display technologies. He has supervised on these topics 18 Ph. D. theses (three honored with the Best Thesis Award), published more than 120 technical articles in major journals (which received more than 4.000 citations), and pronounced invited and keynote presentations in many international meetings. He is also co-inventor of 14 patents, one of them supporting the creation of one Spin-off of the University of Valencia. He is has served in the Program Committee of several Conferences sponsored SPIE, OSA, IEEE. He has been Topical Editor in some O.S.A journals.

Emilio Schez Ortiga received his B.Sc., M.Sc. degree in Photonics, and Ph.D. in Physics from the Faculty of Physics at the University of Valencia (Spain) in 2008, 2009 and 2014, respectively. He has published more than 30 journal papers in the area of Optics and Photonics, and he is co-owner of 6 patents. He is also co-author of a chapter book, and contributed to more than 40 works presented in international conferences. He is also a founding associate of Digital Optical Imaging Technologies, S.L., spin-off company of the University of Valencia.